Computational Analysis of the Reacting Flow in a Microstructured Reformer Using a Multiscale Approach

Alireza T. Naseri and Brant A. Peppley
Fuel Cell Research Centre and Dept. of Chemical Engineering, Queen's University, Kingston, ON K7L 5L9

Jon G. Pharoah
Fuel Cell Research Centre and Dept. of Mechanical Engineering, Queen's University, Kingston, ON K7L 5L9

DOI 10.1002/aic.14411
Published online March 3, 2014 in Wiley Online Library (wileyonlinelibrary.com)

A multiscale methodology is presented to analyze the transport and reaction processes in the catalyst coating of a microstructured reformer and to elucidate the effect of catalyst morphology on transport limitations and the reformer performance. This analysis includes three-dimensional simulations of methane steam reforming at both reactor level (macroscale) and catalyst microstructure level (microscale). Hypothetical catalyst microstructures are generated using an in-house particle packing code. Based on the generated structures, the effective transport properties of the porous catalyst and the average reaction rates in the microstructure are determined to be applied in the pseudohomogeneous model used in the macroscale simulation. Parametric study is done to demonstrate the significant effect of the catalyst intraparticle and interparticle porosity as well as the particle size on the reaction effectiveness factor and methane conversion. This study shows that an optimal catalyst coating has a decreasing porosity along the reformer length based on the difference in the degree of diffusion limitation. © 2014 American Institute of Chemical Engineers *AIChE J*, 60: 2263–2274, 2014

Keywords: multiscale analysis, reformer, catalyst morphology, microstructure

Introduction

Fuel cells are promising candidates for clean electricity generation in a wide range of applications. Efficient production of hydrogen is crucial to reduce the overall cost of electricity generation in fuel cell systems. Catalytic reforming of hydrocarbons in microstructured reactors is an attractive option for this purpose. In the late 1990s, there was a significant increase in the popularity of small-scale reaction engineering and fabrication of microstructured reactors.[1] Since then, a few comprehensive reviews have been written, which study different aspects of the reacting flow in these reactors.[2–4] Microstructured reactors have channels with dimensions in micron to millimeter range that enhance heat and mass transfer and show minimum residence time distribution compared to conventional packed-bed reactors.[3] These reactors could be categorized based on the type of the catalytic bed as either micropacked or coated-wall reactors.[3] Most of the simulations done on microstructured reactors assume only a pseudohomogenous model for the porous catalyst to study the transport and reaction processes. In recent years, the focus has changed and is moving toward detailed multiscale modeling of the catalytic reactors, taking into account the effect of the catalyst morphology on the reactor performance.[5–8] Due to the high rate of the steam reforming reaction, especially near the inlet of the reformer, diffusion limitations may occur which are important and affect this type of reactor's performance. Multiscale modeling offers a new approach to address this problem and to provide solutions based on changing the porous structure of the selected catalyst.

Virtual reconstruction of the catalyst can be used to incorporate the effect of the catalyst structure in the multiscale analysis. One way is the numerical reconstruction of the catalyst using computer codes.[9–13] The other way is the reconstruction based on advanced imaging techniques such as focused ion beam-scanning electron microscopy[14,15] and x-ray computed microtomography.[16,17] Although the real morphology of the catalyst cannot be presented through the numerical reconstruction process, it is possible to generate complex structures that can capture essential characteristics of the real material, calculate the effective transport properties, and simulate the reaction and transport processes in the reconstructed medium.[5,7,8] In this work, based on the computer-generated structures the effective transport properties of the catalyst as well as the reacting flow in the microstructure are simulated. This approach is useful in studying the effects of morphological characteristics like porosity, mean pore size, and particle size on the catalyst performance and can serve as a practical tool for the optimization of the porous structure.

The aim of this work is to demonstrate a methodology for multiscale analysis of the reacting flow in the catalyst coating of a microstructured reformer using computational fluid

Correspondence concerning this article should be addressed to B. A. Peppley at brant.peppley@chee.queensu.ca.

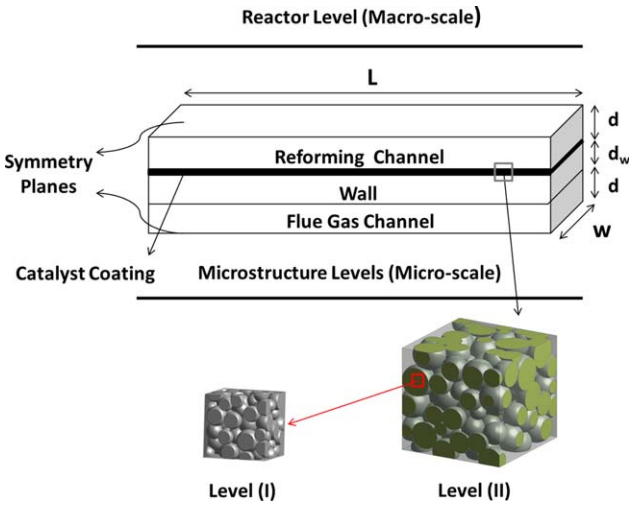

Figure 1. Reactor modeling framework (the spheres are catalyst particles surrounded by the pore domain).

[Color figure can be viewed in the online issue, which is available at wileyonlinelibrary.com.]

dynamics software; ANSYS FLUENT®. This methodology presents a systematic approach to study the relationship between the catalyst structure, effective transport properties, and the catalyst performance in a reformer. The intrinsic kinetic model suggested by Xu and Froment[18] based on Ni/$MgAl_2O_4$ catalyst for methane steam reforming is used in the simulations. The effects of the catalyst porosity, mean particle size, and pore size on the reforming reaction effectiveness factor and methane conversion are elucidated.

Methodology

In this work, models for reaction and transport processes that occur at different length scales are coupled through an iterative procedure. The proposed modeling framework consists of the simulation of the reacting flow at the reactor level, which is defined here as the macroscale model and the calculation of the effective transport properties as well as the simulation of the reacting flow in the catalyst microstructure, which is defined here as the microscale model.

The computer reconstruction of the porous catalyst is based on the drop and roll algorithm explained by Kenney et al.[19] This algorithm generates packing of overlapping spherical particles with specified porosity and Gaussian particle-size distribution. As shown in Figure 1, the catalyst reconstruction is done at two levels. Hypothetical catalyst microstructures are generated, based on the assumption that the catalyst is an agglomeration of spherical particles [Level (II)].The porous structure of each particle is also taken into account by assuming that it is an aggregate of smaller spherical particles [Level (I)]. The calculation of the effective diffusivity and conductivity is done at both levels. The effective transport properties are used in the reacting flow simulation at both microscale and macroscale models. Reacting flow simulation at microscale is only done at one level (Level (II) in Figure 1).

The reactor consists of a reforming channel and a flue gas channel which provides the heat for the endothermic reforming reaction (Figure 1). To incorporate the effect of the catalyst morphology on the reaction rate in the pseudo-homogeneous model at macroscale, the kinetic model should be adjusted to give the same average reaction rate as obtained from the microscale simulation. The procedure starts from the calculation of the effective transport properties for the catalyst coating. Then, these properties are used in the reacting flow simulation at macroscale to obtain the exact concentrations of the mixture components at the catalyst interface with the free stream in the reforming channel as well as the temperatures across the coating. These temperatures and concentrations are used as boundary values for the microscale simulation. The volume-averaged reaction rates in the microstructure obtained from microscale simulation is transferred back to the macroscale simulation to adjust the kinetic model and to fully couple the models with respect to both kinetics and transport. In the following sections, the details of the effective properties calculation, macroscale and microscale simulations, and the coupling procedure are discussed.

Effective transport properties

The calculation of the effective transport properties has a major impact on predicting the performance of a porous medium and it has been a challenging industrial problem. To calculate the effective properties for a porous medium, some information regarding its morphology is required. Morphology consists of two parts: geometry and topology.[10] Geometry refers to the shape and size of the particles and topology refers to the connectivity in the porous medium.[10] According to Sahimi et al.,[20] there are several methods that could be used to obtain the effective properties for disordered porous media. These methods include but are not limited to direct Monte Carlo simulation, random walk method, and effective medium approximation.[20] In addition to these methods, continuum-based numerical techniques could be used to solve the transport equations for digitally reconstructed porous media followed by volume averaging to determine the effective transport properties.[5,21–24]

In this work, effective transport properties are obtained by using the numerical approach (finite-volume method), which involves the solution of the transport equations in the porous structure and using the appropriate transport laws to determine the effective properties.

Effective Diffusivity and Conductivity. All the generated structures are polydisperse assemblies of overlapping spherical particles. Each structure consists of two domains: pore and particle (Figure 2).

The mesh for the geometry is generated in such a way that each unit cell (voxel) is only inside one of the two domains (pore or particle). The mass transfer in the computational domain (Figure 2) could be modeled by using a simple diffusion equation

$$\nabla.(-D\ \nabla c)=0 \tag{1}$$

where D is the diffusivity and c is the concentration. Because a finite-volume method is used by ANSYS FLUENT®,[25] Eq. 1 is integrated and the volume integral is replaced by the surface integral using the divergence theorem

$$\iiint_V \nabla.(-D\ \nabla c)\ dV=\oiint_A (-D\ \nabla c).\boldsymbol{n}\ dA=0 \tag{2}$$

where V is the volume of each unit cell, A is the boundary surface area of the cell, and $\boldsymbol{n}$ is the outward normal vector.

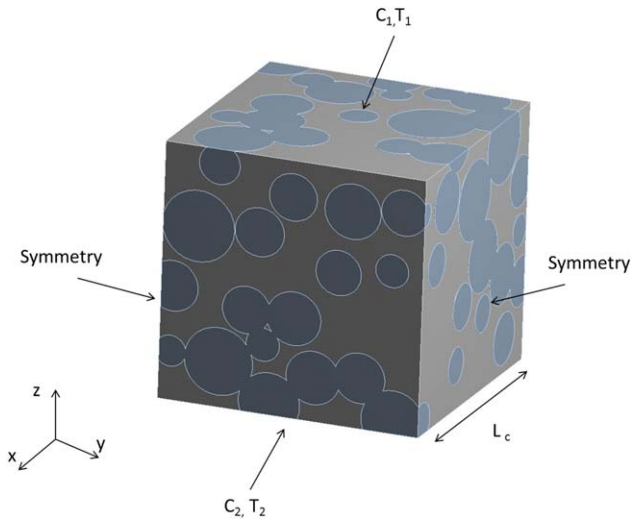

Figure 2. Computer-generated structure with suitable boundary conditions for the calculation of effective diffusivity and conductivity (circles are spherical particles surrounded by the pore domain).

[Color figure can be viewed in the online issue, which is available at wileyonlinelibrary.com.]

Equation 2 is solved for each control volume (voxel) in the pore and particle domain using the respective diffusivity. For the boundary conditions, two concentrations are imposed at the z direction while "symmetry" (zero flux) conditions are imposed at other sides of the cube (Figure 2). After solving Eq. 2, the concentration profile in the computational domain is obtained which then could be used to calculate the mass flux

$$j=\frac{1}{{L_c}^2}\int_{x=0}^{x=L}\int_{y=0}^{y=L}-\left(\frac{\partial c}{\partial z}\right)_{z=0}dxdy \tag{3}$$

The effective diffusivity is determined by using the Fick's Law

$$D_{\text{eff}}=-\frac{j}{\Delta c/L_c} \tag{4}$$

where Δc is the concentration difference in z direction and L_c is the domain length.

The same procedure should be repeated for the other two directions (x and y) to check for anisotropy. Anisotropy is the dependence of the material properties on direction.[11] Diffusivity and conductivity can be viewed as 3×3 tensors that relate the flux, which is a vector, to the gradient of the respective intensity field. For an isotropic porous medium, the nondiagonal elements of the property tensor are zero and all the diagonal elements are equal.[11] For an orthotropic medium, the diagonal elements are different and nondiagonal elements are all zero.[11]

In this work, the effective diffusivities and conductivities are calculated at two steps: first for the particle within the coating microstructure [Level (I)] and then for the microstructure [Level (II)] as shown in Figure 1. The solid phase consists of $Ni/MgAl_2O_4$ particles. To calculate the effective diffusivity of a single catalyst particle, a hypothetical structure is generated. First, a modified version of the diffusion equation is solved considering the Knudsen effect, with the same boundary conditions as shown in Figure 2. The modified diffusivity (D_{mod}) including the Knudsen effect[26] can be written as

$$\frac{D_{\text{mod}}}{D}=\frac{1}{1+\text{Kn}} \tag{5}$$

where Knudsen number is defined as

$$\text{Kn}=\frac{\lambda}{d_{\text{pore}}} \tag{6}$$

and the diffusion equation (Eq. 1) is changed to

$$\nabla.(-D_{\text{mod}}\ \nabla C)\ =\ 0 \tag{7}$$

In Eq. 6, λ is the mean free path of the gas molecule and d_{pore} is the characteristic pore length. The characteristic length is calculated using the mean chord length

$$d_{\text{pore}}=\left(\frac{\langle l^2\rangle}{2\langle l\rangle^2}-\beta\right)\langle l\rangle \tag{8}$$

$$\langle l\rangle=\frac{4V_{\text{pore}}}{S} \tag{9}$$

where V_{pore} is the pore volume and S is the surface area, $\langle l\rangle$ is the mean chord length of the pore domain, and $\beta = 4/13$ as explained by Berson et al.[26] After solving Eq. 7 for the specified structure, the mass flux is calculated and Eq. 4 is used to determine the effective diffusivity. Hydrogen is chosen as the fluid in the pore domain for the properties calculations. The porosity (ε_{I}) to tortuosity (τ_{I}) ratio of a catalyst particle [Level (I) in Figure 1], which is the porous structure geometrical factor ($G_{\text{I},D}$) is equal to the normalized effective diffusivity

$$G_{\text{I},D}=\frac{\varepsilon_{\text{I}}}{\tau_{\text{I}}}=\frac{D_{\text{I,eff}}}{D}(1+\text{Kn}) \tag{10}$$

After calculating the effective diffusivity in the catalyst particle ($D_{\text{I,eff}}$), the diffusion equation is solved for the catalyst coating microstructure [Level (II) in Figure 1]. In this case, the diffusion coefficient in Eq. 1 has two values: one is the molecular diffusivity which is applied in the interparticle void and the other is the effective diffusivity in the particle zone ($D_{\text{I,eff}}$). The overall normalized effective diffusivity gives the overall geometrical factor $G_{\text{II},D}$

$$\frac{D_{\text{II,eff}}}{D}=G_{\text{II},D} \tag{11}$$

The factor $G_{\text{II},D}$ is then used to calculate the effective diffusivity in the reacting flow simulation at macroscale for the specified microstructure. In this way, both intraparticle (ε_{I}) and interparticle (ε_{II}) porosity for the catalyst coating are taken into account and the total porosity ($\varepsilon_{\text{T}}=\varepsilon_{\text{II}}+(1-\varepsilon_{\text{II}})\varepsilon_{\text{I}}$) is used for the macroscale simulation.

In the reacting flow simulation, D in Eq. 11 is the molecular diffusivity of the species "i" in the gas mixture. Hence

$$\frac{D_{i,\text{eff}}}{D_{i,m}}=G_{\text{II},D} \tag{12}$$

where $D_{i,m}$ is calculated by

$$D_{i,m}=\frac{1-X_i}{\sum\limits_{i\neq j}^{N}\frac{X_j}{D_{ij}}} \tag{13}$$

In this equation, X_i is the mole fraction of the species and D_{ij} is the binary diffusivity and is obtained from the Fuller's equation[27]

Table 1. Morphological Characteristics of the Particles in the Catalyst Microstructure (Level I): Intraparticle Porosity (ε_I), Mean Particle Diameter ($\bar{d}$), and Characteristic Pore Length (d_{pore})

Particle Structure	ε_I	$\bar{d} \pm \sigma$ (μm)	d_{pore} (μm)
A	0.23	2.5 ± 0.5	0.240
B	0.3	2.5 ± 0.5	0.515

$$D_{ij} = \frac{10^{-7} \times T^{1.75} \left(\frac{1}{M_i} + \frac{1}{M_j}\right)^{0.5}}{P\left(\left(\sum_k V_{k,i}\right)^{\frac{1}{3}} + \left(\sum_k V_{k,i}\right)^{\frac{1}{3}}\right)} \tag{14}$$

where M_i is the molecular weight, $V_{k,i}$ is the diffusion volume of the species, T is temperature, and P is the system pressure.

A similar procedure is applied to obtain the effective conductivity. The mass diffusion equation and flux are replaced with the conduction equation and heat flux (q)

$$\nabla.(-k\ \nabla T) = 0 \tag{15}$$

$$q = \frac{1}{{L_c}^2} \int_{x=0}^{x=L} \int_{y=0}^{y=L} -\left(\frac{\partial T}{\partial z}\right)_{z=0} dxdy \tag{16}$$

First, the effective conductivity of a single particle ($k_{I,eff}$) is calculated and then the overall effective conductivity of the microstructure ($k_{II,eff}$). By using the Fourier's law of conduction

$$k_{eff} = -\frac{q}{\Delta T / L_c} \tag{17}$$

The overall effective conductivity is calculated and its normalized value is used for the reacting flow simulation

$$\frac{k_{II,eff}}{k_{I,eff}} = G_{II,k} \tag{18}$$

where $k_{I,eff}$ is the effective thermal conductivity of the particle calculated at Level I.

In this work, two structures were generated representing the intraparticle morphology (Table 1). Each side of the cube representing the particle structure is 10 μm. The normalized effective diffusivity and conductivity for the particles (normalized by the modified molecular diffusivity D_{mod} and the solid particle conductivity k_s) are shown in Table 2. Based on the particle morphologies A and B in Table 1, the structures and the overall normalized effective properties (normalized by the molecular diffusivity D and particle effective conductivity $k_{I,eff}$) for the catalyst coating were calculated as shown in Tables 3 and 4. The size of the cube representing the coating microstructure is $100 \times 100 \times 100$ μm.[3]

The effect of the interparticle porosity (ε_{II}) can be observed in Table 4 by comparing the arithmetic average of the normalized diffusivities and conductivities ($\bar{G}_{II,D}$,$\bar{G}_{II,k}$) at the three directions, for the first four structures in Table 3. This indicates that, after increasing the interparticle porosity the overall effective diffusivity increases and the overall effective conductivity decreases. Intraparticle porosity (ε_I) has also a similar effect as shown by the effective properties of the fourth and fifth structures.

Structures 3 and 6 have similar porosity but different particle diameters, despite the significant difference in the characteristic pore length, their effective diffusivities are close to each other while the difference in effective conductivities is more significant. This shows that by keeping the porosity constant the change in particle size has less effect on the effective diffusivity than on the conductivity.

Macroscale model

At the macroscale, a three-dimensional (3-D) computational fluid dynamics simulation was performed (Figure 1). The gas mixture consists of six species (CH_4, H_2O, CO, CO_2, H_2, and N_2). In this work, the widely used intrinsic kinetic model suggested by Xu and Froment[18] was implemented in the simulation based on a catalyst with a composition of 15.2% $Ni/MgAl_2O_4$. In the future, other kinetic models could also be tested in our 3-D geometries such as the detailed microkinetic models[28,29] available for methane steam reforming. The reactions chosen for the simulations are

$$CH_4 + H_2O \rightleftarrows CO + 3H_2,\ \Delta H = 206\ \text{kJ/mol} \tag{19}$$

$$CO + H_2O \rightleftarrows CO_2 + H_2,\ \Delta H = -41\ \text{kJ/mol} \tag{20}$$

$$CH_4 + 2H_2O \rightleftarrows CO_2 + 4H_2,\ \Delta H = 165\ \text{kJ/mol} \tag{21}$$

The respective kinetic expressions are

$$r_1 = \frac{\frac{k_1}{p_{H_2}^{2.5}}\left(p_{CH_4}\, p_{H_2O} - \frac{p_{H_2}^3 p_{CO}}{K_{e,1}}\right)}{(\text{Den})^2} \tag{22}$$

$$r_2 = \frac{\frac{k_2}{p_{H_2}}\left(p_{CO}\, p_{H_2O} - \frac{p_{H_2} p_{CO_2}}{K_{e,2}}\right)}{(\text{Den})^2} \tag{23}$$

$$r_3 = \frac{\frac{k_3}{p_{H_2}^{3.5}}\left(p_{CH_4} {p_{H_2O}}^2 - \frac{p_{H_2}^4 p_{CO_2}}{K_{e,3}}\right)}{(\text{Den})^2} \tag{24}$$

$$\text{Den} = 1 + K_{CO} p_{CO} + K_{H_2} p_{H_2} + K_{CH_4} p_{CH_4} + K_{H_2O} \frac{p_{H_2O}}{p_{H_2}} \tag{25}$$

The kinetic model and parameters for the three reactions: steam reforming (Eq. 19), water–gas shift (Eq. 20), and reverse methanation (Eq. 21) were obtained from Zanfir and Gavriilidis.[30] The kinetic model is coded as a user-defined function (UDF) in ANSYS FLUENT®.

In the reforming and flue gas channels the continuity equation, species mass, momentum, and energy conservation equations with the ideal gas law (equation of state) are solved at steady state. The equations are[31]

Table 2. Effective Diffusivity and Conductivity of the Two Particle Structures (A and B) in the Catalyst Microstructure; $\bar{G}_{I,D}\bar{G}_{I,k}$ are the Average of the Properties in *x*, *y*, and *z* Direction

Structure	x:$D_{I,eff}/D_{mod}$	y:$D_{I,eff}/D_{mod}$	z:$D_{I,eff}/D_{mod}$	$\bar{G}_{I,D}$	x:$k_{I,eff}/k_s$	y:$k_{I,eff}/k_s$	z:$k_{I,eff}/k_s$	$\bar{G}_{I,k}$
A	0.071	0.071	0.08	0.074	0.63	0.60	0.671	0.631
B	0.156	0.110	0.164	0.143	0.47	0.463	0.425	0.452

Table 3. Morphological Characteristics of the Catalyst Coating Microstructure (Level II): Interparticle Porosity (ε_{II}), Mean Particle Diameter ($\bar{d}$), and Characteristic Pore Length (d_{pore})

Structure	Particle Structure	ε_{II}	$\bar{d} \pm \sigma$ (μm)	d_{pore} (μm)
1	B	0.14	25 ± 5	1.3
2	B	0.23	25 ± 5	2.52
3	B	0.3	25 ± 5	4.98
4	B	0.36	25 ± 5	6.09
5	A	0.36	25 ± 5	6.14
6	B	0.3	16.66 ± 3.3	2.43

$$\nabla.(\rho\mathbf{v})=0 \tag{26}$$

$$\nabla.(\rho Y_i\mathbf{v})=-\nabla.\mathbf{j}_i+r_i \tag{27}$$

$$\nabla.(\rho\mathbf{v}\mathbf{v})=-\nabla P+\nabla.\left[\mu(\nabla\mathbf{v}+\nabla\mathbf{v}^T)-\frac{2}{3}\mu\nabla.\mathbf{v}\mathbf{I}\right]+\mathbf{F} \tag{28}$$

$$\nabla.(\rho h\mathbf{v})=\nabla.(k\nabla T-\sum_i h_i\mathbf{j}_i)+S_h \tag{29}$$

$$P=\rho RT\sum_i\frac{Y_i}{M_i} \tag{30}$$

where ρ is the density, $\mathbf{v}$ is the velocity, Y_i is the mass fraction of the species "i" in the mixture, $\mathbf{j}_i$ is the diffusive mass flux, and r_i is the rate of reaction of the species "i," μ is the viscosity, P is the pressure, $\mathbf{I}$ is the unit tensor, and $\mathbf{F}$ is the momentum source term, k is the thermal conductivity, h_i is the specific enthalpy of the species "i," S_h is the heat of reaction, and M_i is the molecular weight of the species. The reaction term r_i in Eq. 27, $\mathbf{F}$ in Eq. 28, and S_h in Eq. 29 only appear in the porous catalyst domain. The transport properties are replaced with the effective properties for the porous domain. The diffusive mass flux term $\mathbf{j}_i$ in Eq. 27 can be modeled by using the Fick's law with the effective diffusivity of the species in the coating

$$\mathbf{j}_i=-\rho D_{i,\text{eff}}\nabla Y_i \tag{31}$$

Boundary Conditions and Solver. The inlet temperatures, compositions, and mass flow rates are specified in ANSYS FLUENT® for both reforming and flue gas channels. The inlet diffusion is also assumed for both channels. The "pressure outlet" condition is used for the channels exit. Mass, energy continuity, and zero velocity are assumed at the interface of the catalyst coating with the free stream in the reforming channel and the zero mass flux condition is specified at the interface of the wall and the channels. At the center of the channel, "symmetry" boundary condition is assumed. Nominal values of the process parameters for the reactor simulation are shown in Table 5. These input values are kept constant for all the simulations unless otherwise stated. Based on the process parameters, the flow is laminar in both channels. Reynolds number in the reforming channel and flue gas channel is around 2 and 8, respectively. The pressure-based segregated solver is used with the SIMPLE scheme for pressure-velocity coupling, PRESTO for pressure interpolation, and second-order upwind scheme for the species transport, energy, and momentum equations.

Table 5. Nominal Values for the Parameters in the Macroscale Simulations

Reforming Channel	Value
Inlet mass flow rate	1×10^{-7} kg/s
Inlet velocity	0.80 m/s
Inlet temperature	700 K
Half channel gap size (d)	400 μm
Steam to carbon ratio	3.4
Gas hourly space velocity (GHSV)	197064 1/h
Inlet composition (mole fraction)	
CH_4	0.21
H_2O	0.71
CO_2	0.0119
H_2	0.026
N_2	0.0421
Wall	
Wall thickness (d_w)	800 μm
Wall thermal conductivity	16 W/m/K
Flue gas channel	
Inlet mass flow rate	4×10^{-7} kg/s
Inlet velocity	2.7 m/s
Inlet temperature	1400 K
Inlet composition (mole fraction)	
CO_2	0.3
H_2O	0.6
N_2	0.1
Half channel gap size (d)	400 μm
Catalyst coating thickness	100 μm
Reactor length (L)	2 cm
Width of the Channels (w)	1 mm
Pressure	1 atm

Microscale model

After running the simulation at macroscale, the species concentrations and temperatures at the interface of the catalyst coating with the free stream, are used as inputs (inlet boundary conditions) for the reacting flow simulation in the microstructure (Figure 3). The domain size for the computer-reconstructed microstructure is $100 \times 100 \times 100$ μm^3. Representative simulations in the coating microstructure are done based on six points selected along the reactor length. This approach is used to ensure that the procedure is computationally practical also sufficiently accurate. At these six points along the reactor, the concentrations and temperatures at the interface with the free stream are averaged over the width (x direction) to take into account their variations and then used as the boundary conditions for the microscale simulations. As shown in Figure 3, the sides of the cube have symmetry (zero flux) boundary condition and the bottom, which is at the wall, has zero mass flux and constant temperature. The microstructure consists of two domains: particle and pore. Catalyst particles are assumed to be porous with geometrical factors (G) calculated as discussed before. The pore domain contains the

Table 4. Overall Effective Diffusivity and Conductivity of the Generated Structures

Structure	x:$D_{II,eff}/D$	y:$D_{II,eff}/D$	z:$D_{II,eff}/D$	$\bar{G}_{II,D}$	x:$k_{II,eff}/k_{I,eff}$	y:$k_{II,eff}/k_{I,eff}$	z:$k_{II,eff}/k_{I,eff}$	$\bar{G}_{II,k}$
1	0.189	0.197	0.188	0.191	0.752	0.747	0.73	0.743
2	0.235	0.254	0.227	0.238	0.521	0.51	0.502	0.511
3	0.235	0.259	0.243	0.245	0.302	0.314	0.372	0.329
4	0.301	0.292	0.289	0.294	0.282	0.21	0.283	0.258
5	0.276	0.294	0.292	0.287	0.411	0.486	0.483	0.46
6	0.27	0.221	0.294	0.261	0.389	0.402	0.45	0.413

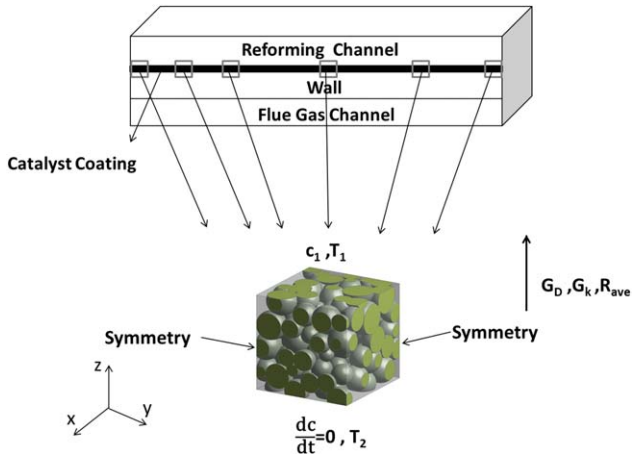

Figure 3. Data transfer between macroscale and microscale model.

[Color figure can be viewed in the online issue, which is available at wileyonlinelibrary.com.]

gas mixture where bulk properties are used. The methane steam reforming reaction occurs in the porous particles. It is assumed that diffusion is the dominant mechanism of mass transfer inside the catalyst coating; therefore, a nonisothermal diffusion-reaction model is solved for the microstructure. It is possible to verify this assumption by using the Peclet number (Pe), which shows the ratio of the rate of convection to the rate of diffusion[32]

$$\mathrm{Pe} = \frac{v d_{\mathrm{pore}}}{D} \tag{32}$$

where v is the physical velocity, d_{pore} is the characteristic pore length, and D is the molecular diffusivity. For all the structures, the range of species diffusivities and the flow rates used in the simulations, the Peclet number is much less than one ($\mathrm{Pe} < 1$), which means that diffusion is the dominant mechanism for mass transfer in the porous catalyst. The equations solved at microscale are

$$\nabla . \mathbf{j}_i = r_i \tag{33}$$

$$\nabla . (k \nabla T - \sum_i h_i j_i) + S_{\mathrm{h}} = 0 \tag{34}$$

To match the simulations at both scales, momentum equation is not solved for the porous catalyst at macroscale either. The reactions (Eqs. 19–21) occur in the catalyst particles. The kinetic model and the transport properties are implemented through UDFs in ANSYS FLUENT®. In the pore domain between particles, molecular diffusivity is used according to Eq. 13 and in the intraparticle pores, the effective diffusivity of the species is used considering the Knudsen diffusion (Eq. 10). As for the thermal conductivity, in the pore domain the conductivity of the gas mixture and in the particles domain the effective conductivity of the porous particle is used. Various approaches could be used to couple the microscale and macroscale models with respect to kinetics. One way is to use regression analysis at both microscale and macroscale to fit the average reaction rates at six points along the reactor length. A spline curve fitting methodology[33] using piece-wise polynomials could be used for this purpose. The ratio of the average of the fitted function at microscale to the average of the function at macroscale can be used as a coefficient to modify the kinetic model in the macroscale simulation. Instead of regression an easier way is to use weighted moving average, giving more weights to the points near the reactor inlet where most of the reaction occurs. This method gives a similar result to the regression method with minimal difference. Weighted moving average is defined for N points as

$$\overline{R}_{\mathrm{ave}} = \frac{N \times R_{\mathrm{ave},1} + (N-1) \times R_{\mathrm{ave},2} + \ldots + 1 \times R_{\mathrm{ave},N}}{N + (N-1) + \ldots + 1} \tag{35}$$

for $N = 6$, Eq. 35 becomes

$$\overline{R}_{\mathrm{ave}} = \frac{6 \times R_{\mathrm{ave},1} + 5 \times R_{\mathrm{ave},2} + 4 \times R_{\mathrm{ave},3} + 3 \times R_{\mathrm{ave},4} + 2 \times R_{\mathrm{ave},5} + 1 \times R_{\mathrm{ave},6}}{6+5+4+3+2+1} \tag{36}$$

where $R_{\mathrm{ave},N}$ is the volume-averaged reaction rate in the microstructure or the average reaction rate at macroscale at a certain point in the reactor. The $\overline{R}_{\mathrm{ave}}$ calculated from the microscale simulation is divided by the $\overline{R}_{\mathrm{ave}}$ obtained from the macroscale simulation. The ratio is used as a coefficient to modify the kinetic model at the macroscale to take into account the effect of the catalyst structure. As such, Eq. 27 becomes

$$\nabla . (\rho Y_i \mathbf{v}) = -\nabla . \mathbf{j}_i + \frac{\overline{R}_{\mathrm{ave,micro}}}{\overline{R}_{\mathrm{ave,macro}}} r_i \tag{37}$$

Because the macroscale simulation is modified, the concentration and temperature profiles in the reactor are changed as well. This modification affects the microscale simulation results and requires iteration. The iteration termination tolerance is 2% based on the average reaction rate at the micro and macro scale. All the computations in the microstructure are done with the help of the facilities of the Shared Hierarchical Academic Research Computing Network (SHARCNET: www.sharcnet.ca) and Compute/Calcul Canada.

Grid Generation and Convergence

Convergence is a common problem of reacting flow simulations especially in such complex geometries with nonlinear kinetic models. For the cases solved in this work, polyhedral mesh is used for all the structures generated. For this purpose, first a tetrahedral mesh is generated for each structure then the tetrahedral cells are converted to polygonal cells inside ANSYS FLUENT® (Figure 4). A faster convergence

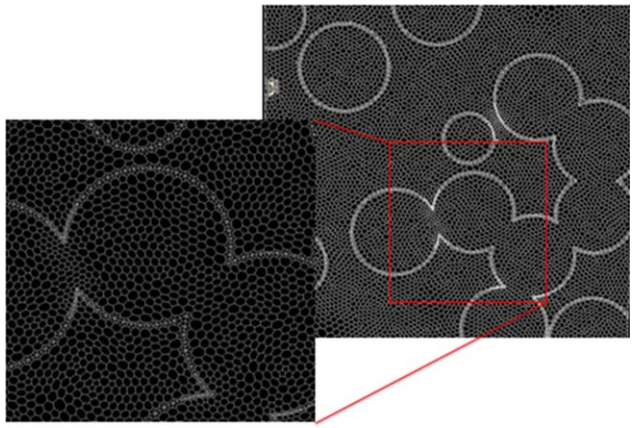

Figure 4. Polyhedral mesh (two-dimensional section of the microstructure shows the overlapping particles).

[Color figure can be viewed in the online issue, which is available at wileyonlinelibrary.com.]

was observed when using polyhedral mesh compared to tetrahedral mesh. A grid independence study was done for the generated structures. The minimum and maximum mesh sizes tested for the structures with larger particles are about 500,000 and 2,000,000 cells and for the structure with smaller particles are 1.5 and 2.7 million cells. All the generated structures with larger particle size have a grid resolution around 1.5 million cells and the one with smaller particle size has a resolution of approximately 2.3 million cells. Increasing the mesh size above, the stated values had a negligible effect on the result (less than 1% change in the species mass fraction surface monitors). As for the convergence criteria, residuals drop to 10^{-7} as well as constant monitored values (species mass fraction and average reaction rate in the catalyst) were considered.

Macroscale Simulation Results

The variation in the steam reforming reaction rate is shown in Figure 5. In Figure 6, the average temperature profiles along the reformer (y direction) on the top and bottom sides of the catalyst coating are shown. It is clear that most of the reforming reaction occurs near the reformer inlet; as a result it is expected that transport limitations will be greater in that region. In the cocurrent mode of operation, the significant temperature gradient close to the reformer inlet provides high heat flux for the endothermic reforming reaction; also the temperature profiles show fast convergence after a few millimeters into the channel. The profiles in Figures 5 and 6 are based on the properties of the structure 3 in Table 3.

Microscale Simulation Results

To identify the effect of the interparticle porosity on the reforming reaction effectiveness factor, a number of simulations were done for structures 1–4 shown in Table 3 (Figure 7). The effectiveness factor is defined here as

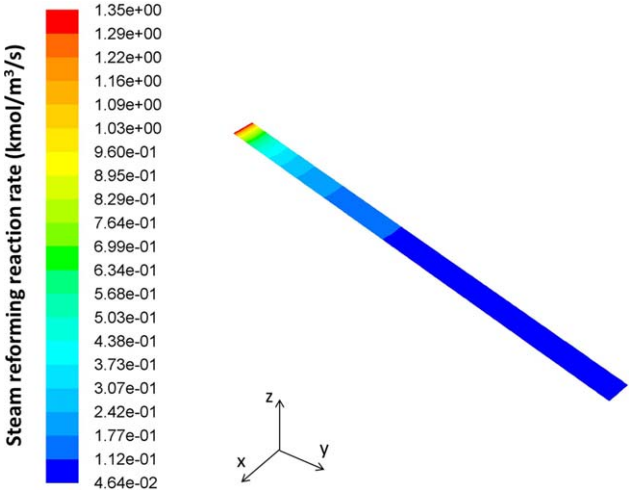

Figure 5. An example of the contour plot for the steam reforming reaction rate (Eq. 19) in the catalyst coating (top view) based on the structure 3 in Table 3.

[Color figure can be viewed in the online issue, which is available at wileyonlinelibrary.com.]

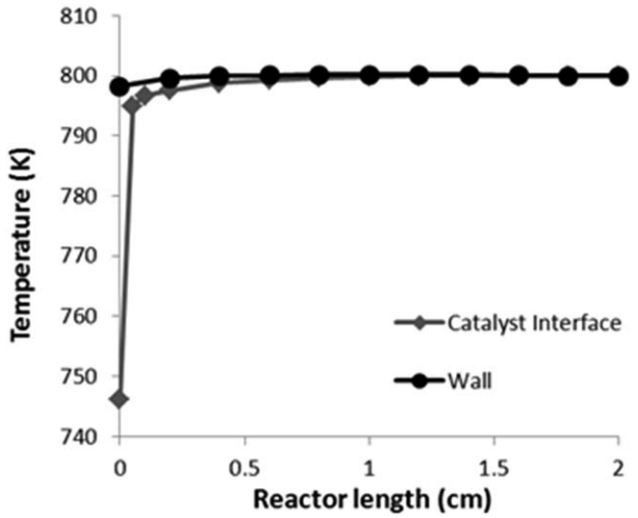

Figure 6. Temperature profiles along the reformer length on the two sides of the catalyst coating based on the structure 3 in Table 3.

$$\eta = \frac{\int_v R dV_p}{R_s V_p} \tag{38}$$

where V_p is the volume of the particles in the microstructure (reactive volume) and R_s is the reaction rate at the interface of the catalyst coating with the free stream. The values for the effectiveness factor are relatively high because of the low temperature in the base case simulation (average wall temperature about 800 K). When the interparticle porosity decreases the effectiveness factor decreases as well, specifically near the reformer inlet. It can be seen that higher porosity and characteristic pore length facilitate species diffusion. Consequently, in the structure with the lowest porosity (0.14), the diffusion limitation is higher and extends more toward the reformer outlet.

The result shown in Figure 7 can be better understood by examining Figures 8–10. These figures show methane mole fraction, reforming reaction rate, and temperature profiles for structures 1 and 4 from Table 3, structure 1 with the highest

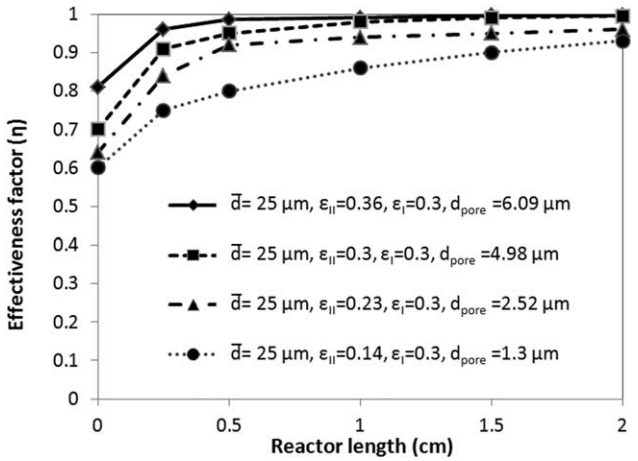

Figure 7. The effect of interparticle porosity on the steam reforming reaction (Eq. 19) effectiveness factor for structures 1–4 in Table 3.

All other parameters are kept at their nominal values shown in Table 5.

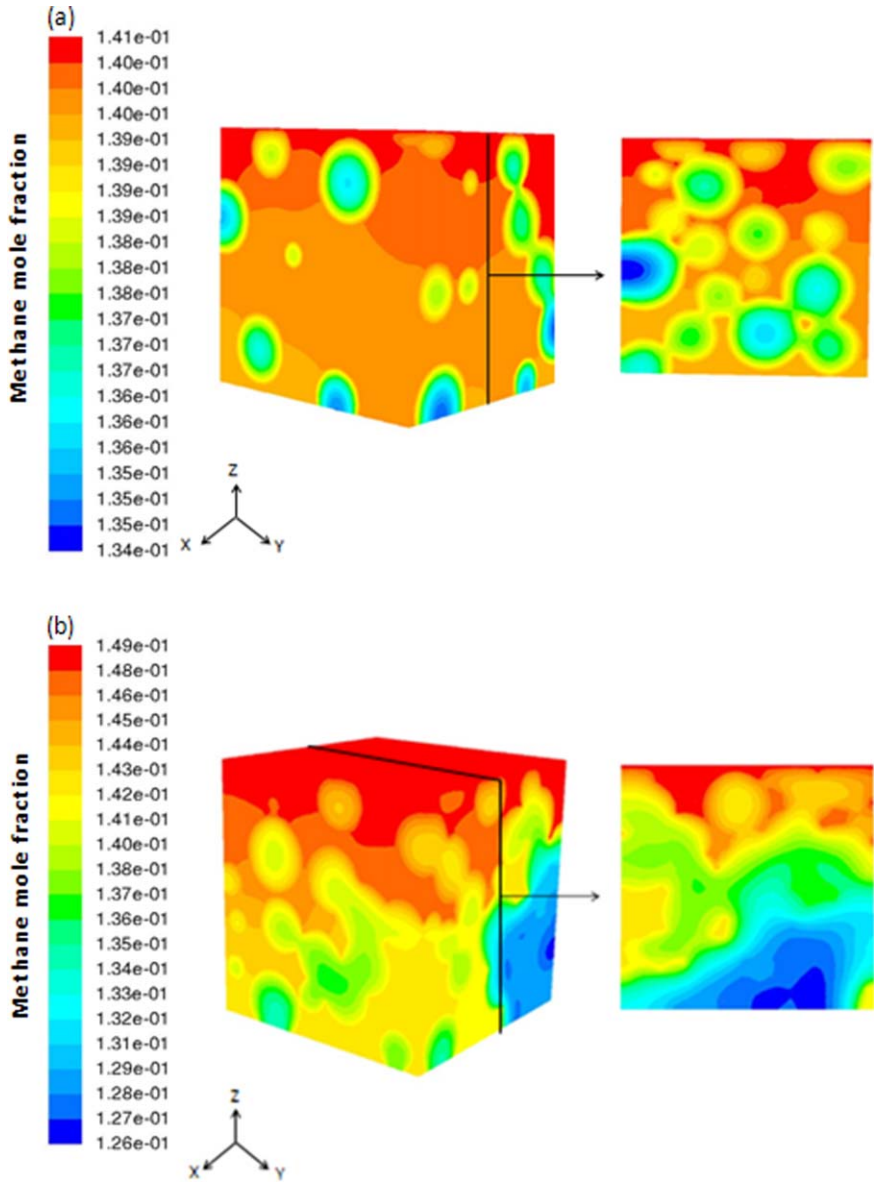

Figure 8. The effect of interparticle porosity on methane mole fraction profile for two microstructures and their respective midplanes at $x = 50$ μm, for a point at 2.5 mm from the reformer inlet: (a) porosity = 0.36 and (b) porosity = 0.14.

Top of the domain is the interface with the free stream and the bottom is the reactor wall. [Color figure can be viewed in the online issue, which is available at wileyonlinelibrary.com.]

and structure 4 with the lowest interparticle porosity. A comparison of the results at a point near the reformer inlet at 2.5 mm into the channel shows the impact of the improved mass diffusion in the structure with the higher porosity (Figure 8). In this structure, significantly larger reaction rates are observed in the microstructure where it is adjacent to the high-temperature wall. By contrast in the structure with the lower porosity (0.14) and higher degree of particles overlaps, the reforming reaction rate in the particles drops significantly over the thickness of the coating (Figure 9).

As for the temperature profiles, the difference between the two structures is not significant and profiles show almost isothermal condition at 2.5 mm into the reactor. No secondary temperature profile or cold spots were observed inside the catalyst particles for all the generated structures for all the selected points in the reformer (Figure 10).

The effect of the mean particle diameter on the effectiveness factor was examined while keeping both intraparticle and interparticle porosity constant. Figure 11 shows a comparison between structures 3 and 6 in Table 3. It can be seen for the particle with lower mean particle size despite the consequential lower characteristic pore length, the effectiveness factor is greater. On one hand, lower pore size hinders mass diffusion in the interparticle void. On the other hand, the diffusion length inside the smaller particles is shorter and the surface area available to the reacting species is larger. The interplay between these factors results in the increase in the effectiveness factor.

The effect of intraparticle porosity on the effectiveness factor for the structures with similar interparticle porosity and mean particle diameter (structures 4 and 5 in Table 3) is shown in Figure 12. The plots show that lower intraparticle

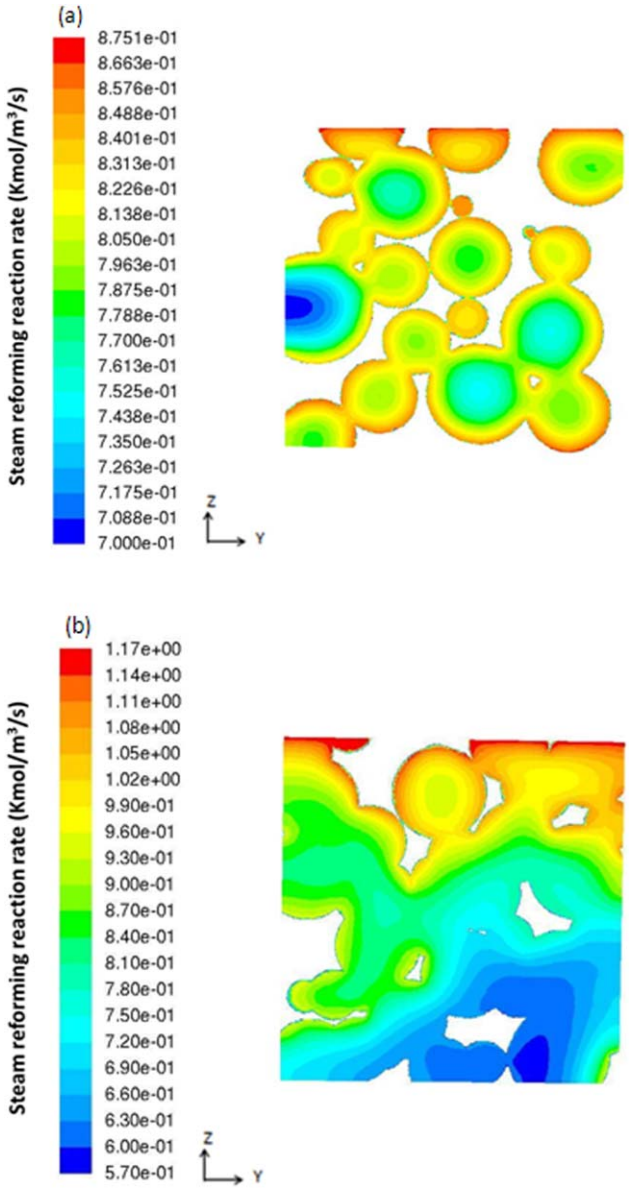

Figure 9. The effect of interparticle porosity on steam reforming reaction rate profiles for two microstructures midplanes at $x = 50$ μm, for a point at 2.5 mm from the reformer inlet: (a) porosity=0.36 and (b) porosity=0.14.

[Color figure can be viewed in the online issue, which is available at wileyonlinelibrary.com.]

porosity increases diffusion limitation and decreases the effectiveness factor.

As for the process temperature, increasing the temperature exacerbates diffusion limitations. Higher temperature increases the rate of the reforming reaction, which results in a reduction in the effectiveness factor (Figure 13).

Multiscale Analysis

The results of the reacting flow simulation in the reformer after coupling macroscale and microscale models are shown in Table 6. In all the simulations, the total catalyst coating volume is constant. The methane conversion for the structures with different interparticle porosity shows a decline when the porosity exceeds 0.3. This is the result of interplay between diffusion and reaction in the microstructure. On one hand, increasing the interparticle porosity facilitates species diffusion between particles. On the other hand, by increasing the void fraction, the amount of catalyst present in the microstructure decreases which may result in a reduction in the average reaction rate. This could also be demonstrated by showing the change in the volume-averaged rate of hydrogen production in the microstructure vs. the interparticle porosity according to all the three reactions (Eqs. 19–21). Because the average reaction rate varies along the reformer, values were obtained based on two points: one near the reformer inlet and one near the outlet. It is expected that diffusion limitation is more severe near the inlet where the reaction rate is higher.

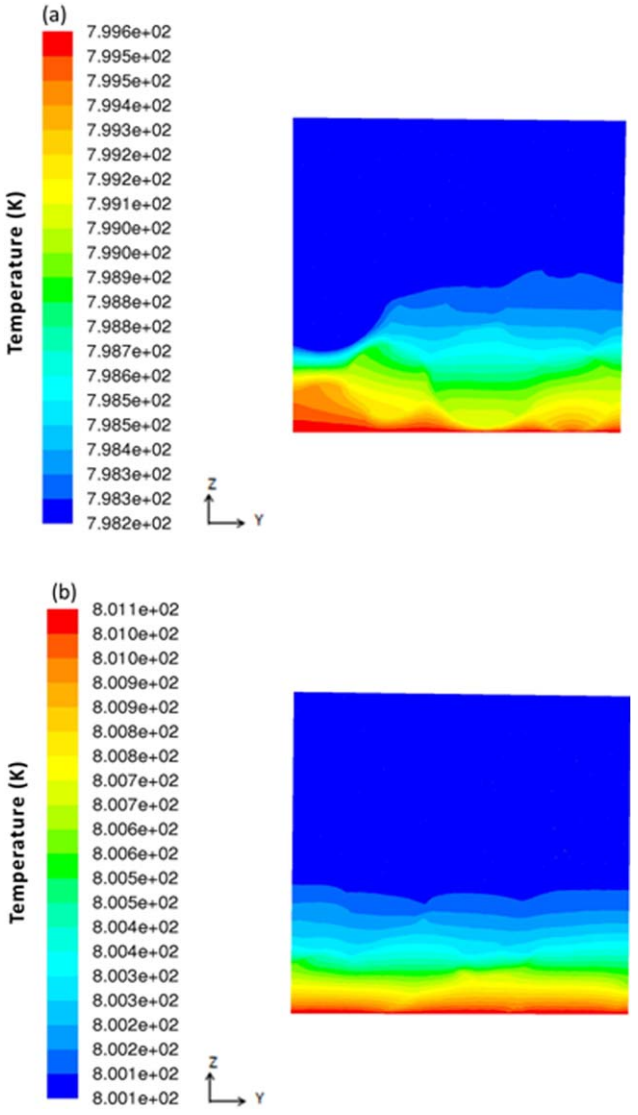

Figure 10. The effect of interparticle porosity on temperature profile for two microstructures mid planes at $x = 50$ μm, for a point at 2.5 mm from the reformer inlet: (a) porosity = 0.36 and (b) porosity = 0.14.

No secondary temperature profile or cold spots were observed inside the catalyst particles for all the generated structures. [Color figure can be viewed in the online issue, which is available at wileyonlinelibrary.com.]

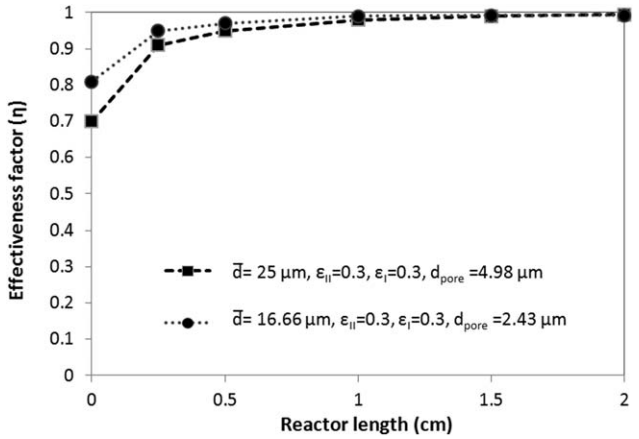

Figure 11. The effect of mean particle diameter on steam reforming reaction (Eq. 19) effectiveness factor for structures 3 and 6 in Table 3.

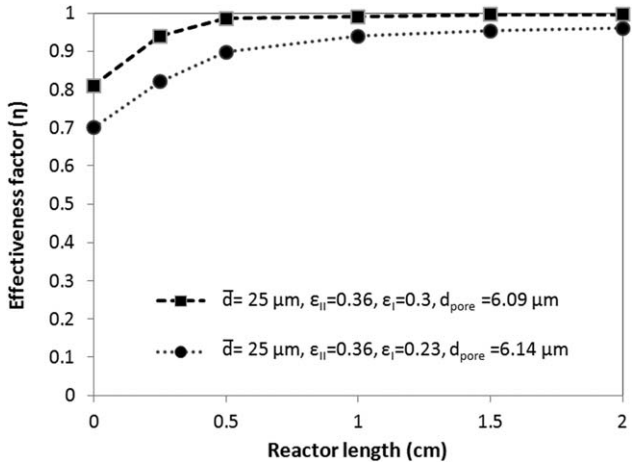

Figure 12. The effect of intraparticle porosity on the steam reforming reaction (Eq. 19) effectiveness factor for structures 4 and 5 in Table 3.

Figure 14 shows the effect of the interparticle porosity on the volume-average rate of hydrogen production for a point near the reformer inlet where the concentrations of methane and water vapor are higher. Based on the structures studied in this work, the plot shows a maximum rate for an interparticle porosity in the range 0.26–0.36. In Figure 15, it can be observed that, for the point near the reformer outlet with lower concentrations of methane and water vapor, the average reaction rate decreases significantly with increasing interparticle porosity.

The results shown in Figures 14 and 15 indicate that for the catalyst coating varying porosity along the reformer length should result in improved performance. Near the

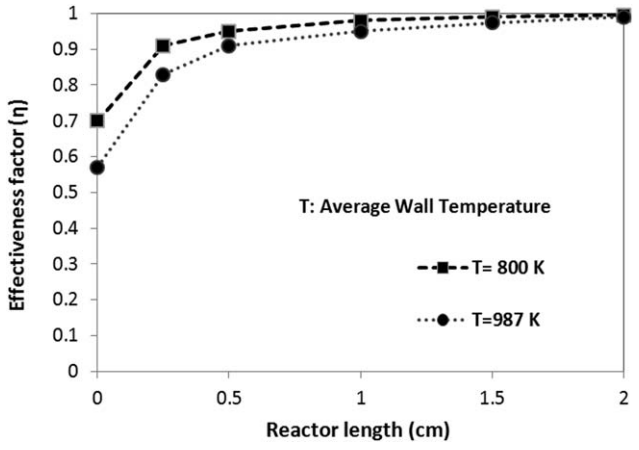

Figure 13. The effect of temperature on the steam reforming reaction (Eq. 19) effectiveness factor for structure 3 in Table 3.

Table 6. The Effect of the Catalyst Structure on Methane Conversion in the Reformer; Interparticle Porosity (ε_{II}), Intraparticle Porosity (ε_I), Mean Particle Diameter ($\bar{d}$)

Structure	ε_{II}	ε_I	$\bar{d} \pm \sigma$ (μm)	Conversion
1	0.14	0.3	25 ± 5	0.4
2	0.23	0.3	25 ± 5	0.45
3	0.3	0.3	25 ± 5	0.47
4	0.36	0.3	25 ± 5	0.42

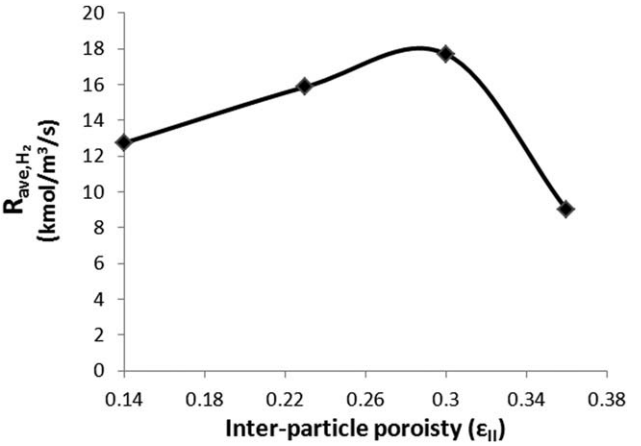

Figure 14. The volume-averaged rate of hydrogen production in the microstructure vs. the interparticle porosity for a point near the reformer inlet (2.5 mm from the inlet or 12.5% of the reactor length).

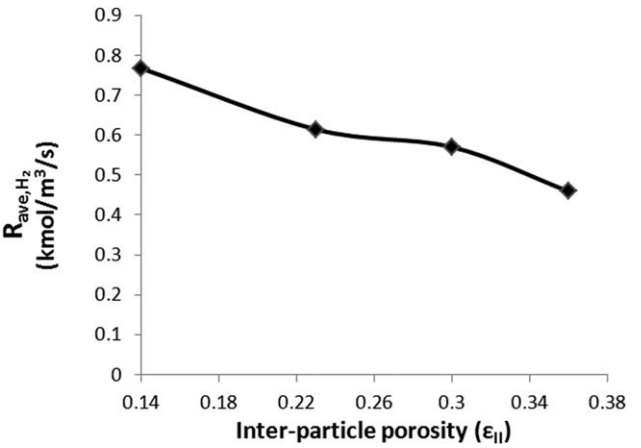

Figure 15. The volume-averaged rate of hydrogen production in the microstructure vs. the interparticle porosity for a point near the reformer outlet (5 mm from the outlet).

reformer inlet, due to the higher rate of the steam reforming reaction, the diffusion limitation is higher; therefore, the void between particles should be larger to facilitate the mass transfer. Conversely, near the reformer outlet, where the reaction rate drops and the hydrogen concentration is higher, the porosity should be reduced to increase the solid fraction of the catalyst.

Conclusions and Outlook

A multiscale modeling framework was presented to analyze the reacting flow in the catalyst coating of a microstructured reformer using the CFD software: ANSYS FLUENT®. This work was focused on incorporating the effect of the catalyst morphology in the reactor simulation by coupling the microscale and macroscale models. It was demonstrated that the catalyst morphological characteristics including the intraparticle and interparticle porosity as well as the particle size have significant impact on the effectiveness factor. It was shown that for a given particle structure, increasing the interparticle porosity increases the reforming reaction effectiveness factor. As for the rate of hydrogen production in the catalyst, near the reformer inlet, where the reforming reaction rate is higher, the rate of hydrogen production increases with increasing porosity but it reaches a maximum around 0.3. Conversely, near the reformer outlet where the reforming reaction rate decreases, the rate of hydrogen production decreases with increasing porosity. This shows the fact an optimal catalyst structure would have decreasing porosity along the reformer length, based on the difference in the degree of diffusion limitation.

The analysis presented in this work could be utilized for a range of porosities and particle sizes to predict the optimal structure of the porous catalyst layer for a given steam reforming process and given kinetic model. Further work is planned to compare the results based on the current particle packing code with the image-based reconstruction of the catalyst to improve the computer reconstruction method and develop reacting flow simulations for more realistic structures.

Acknowledgment

The funding for this project is partially provided by the Natural Sciences and Engineering Research Council of Canada (NSERC) via the Solid Oxide Fuel Cells Canada (SOFCC) Network.

Notation

c = concentration, mol/m^3
$\bar{d}$ = average particle diameter, m
d_{pore} = characteristic length of the pore, m
D = diffusivity, m^2/s
D_{mod} = diffusivity modified by Knudsen number, m^2/s
$D_{I,eff}$ = effective diffusivity in the porous catalyst at Level I, m^2/s
$D_{II,eff}$ = effective diffusivity in the porous catalyst at Level II, m^2/s
G_I, G_{II} = porous structure geometrical factor at Levels I and II (for diffusivity and conductivity)
j_i = diffusion mass flux, kg /m^2/s
k = conductivity, W/m/K
k_s = solid particle conductivity, W/m/K
$k_{I,eff}$ = effective conductivity in the porous catalyst at level I, W/m/K
$k_{II,eff}$ = effective conductivity in the porous catalyst at level II, W/m/K
Kn = Knudsen number
$\langle l \rangle$ = mean chord length of the pore network, m
L_c = porous structure domain length, m
M_i = molecular weight of the species, kg/mol
P = Pressure, Pa
Pe = Peclet number
r_i = species reaction rate, mol/kg$_{cat}$/s
T = temperature, K
$\mathbf{v}$ = velocity, m/s
V_p = particles volume, m^3
X_i = species mole fraction
Y_i = species mass fraction

Greek letters

ε_I = intraparticle porosity
ε_{II} = interparticle porosity
ρ = density, kg/m^3
μ = viscosity, kg/m/s
η = effectiveness factor
τ = tortuosity

Literature Cited

1. Hessel V, Löwe H. Microchemical engineering: components, plant concepts user acceptance–part I. *Chem Eng Technol*. 2003;26:13–24.
2. Kolb G, Hessel V. Micro-structured reactors for gas phase reactions. *Chem Eng J*. 2004;98:1–38.
3. Kiwi-Minsker L, Renken A. Microstructured reactors for catalytic reactions. *Catal Today*. 2005;110:2–14.
4. Hessell V, Knobloch C, Löwe H. Review on patents in microreactor and micro process engineering. *Recent Pat Chem Eng*. 2008;1:1–16.
5. Kosek J, Štěpánek F, Marek M. Modeling of transport and transformation processes in porous and multiphase bodies. *Adv Chem Eng*. 2005;30:137–203.
6. Wang G, Coppens MO. Rational design of hierarchically structured porous catalysts for autothermal reforming of methane. *Chem Eng Sci*. 2010;65:2344–2351.
7. Kočí P, Novák V, Štěpánek F, Marek M, Kubíček M. Multi-scale modelling of reaction and transport in porous catalysts. *Chem Eng Sci*. 2010;65:412–419.
8. Novak V, Koci P, Stepanek F, Marek M. Integrated multiscale methodology for virtual prototyping of porous catalysts. *Ind Eng Chem Res*. 2011;50:12904–12914.
9. Adler PM. *Porous Media: Geometry and Transports*. Oxford: Butterworth-Heinemann, 1992.
10. Sahimi M. *Heterogeneous Materials: Linear Transport and Optical Properties, I*. Vol. 1. New York: Springer-Verlag, 2003.
11. Torquato S, Haslach H Jr. Random heterogeneous materials: microstructure and macroscopic properties. *Appl Mech Rev*. 2002;55:B62.
12. Vidal D, Zou X, Uesaka T. Modelling coating structure development: Monte-Carlo deposition of particles with irregular shapes. *Nord Pulp Pap Res J*. 2004;19:420–427.
13. Vidal D, Bertrand F. Recent progress and challenges in the numerical modeling of coating structure development. *Proceedings of the TAPPI Advanced Coating Fundamentals Symposium*. Atlanta, GA: TAPPI Press, 2006:228–250.
14. Shearing P, Golbert J, Chater R, Brandon N. 3D reconstruction of SOFC anodes using a focused ion beam lift-out technique. *Chem Eng Sci*. 2009;64:3928–3933.
15. Wilson JR, Kobsiriphat W, Mendoza R, Chen HY, Hiller JM, Miller DJ, Thornton K, Voorhees PW, Adler SB, Barnett SA. Three-dimensional reconstruction of a solid-oxide fuel-cell anode. *Nat Mater*. 2006;5:541–544.
16. Izzo JR Jr, Joshi AS, Grew KN, Chiu WKS, Tkachuk A, Wang SH, Yun W. Nondestructive reconstruction and analysis of SOFC anodes using X-ray computed tomography at sub-50 nm resolution. *J Electrochem Soc*. 2008;155:B504.
17. Novák V, Stepánek F, Koci P, Marek M, Kubícek M. Evaluation of local pore sizes and transport properties in porous catalysts. *Chem Eng Sci*. 2010;65:2352–2360.
18. Xu J, Froment GF. Methane steam reforming, methanation and water gas shift: I. *Intrinsic kinetics. AIChE J*. 1989;35:88–96.
19. Kenney B, Valdmanis M, Baker C, Pharoah J, Karan K. Computation of TPB length, surface area and pore size from numerical reconstruction of composite solid oxide fuel cell electrodes. *J Power Sources*. 2009;189:1051–1059.
20. Sahimi M, Gavalas GR, Tsotsis TT. Statistical and continuum models of fluid-solid reactions in porous media. *Chem Eng Sci*. 1990;45:1443–1502.

21. Kočí P, Štěpánek F, Kubíček M, Marek M. Pore-scale modeling of non-isothermal reaction phenomena in digitally reconstructed porous catalyst. *Mol Simul*. 2007;33:369–377.
22. Golbert J, Adjiman CS, Brandon NP. Microstructural modeling of solid oxide fuel cell anodes. *Ind Eng Chem Res*. 2008;47:7693–7699.
23. Salejova G, Grof Z, Solcova O, Schneider P, Kosek J. Strategy for predicting effective transport properties of complex porous structures. *Comput Chem Eng*. 2011;35:200–211.
24. Choi H, Berson A, Pharoah J, Beale S. Effective transport properties of the porous electrodes in solid oxide fuel cells. *Proc Inst Mech Eng A J Power Energy*. 2011;225:183.
25. Ansys, Inc. *ANSYS FLUENT 13.0. Theory Guide*. Canonsburg: Ansys, Inc., 2010.
26. Berson A, Choi HW, Pharoah JG. Determination of the effective gas diffusivity of a porous composite medium from the three-dimensional reconstruction of its microstructure. *Phys Rev E*. 2011; 83:026310.
27. Cussler EL. *Diffusion: Mass Transfer in Fluid Systems*. Cambridge, UK: Cambridge University Press, 1997.
28. Maier L, Schädel B, Delgado KH, Tischer S, Deutschmann O. Steam reforming of methane over nickel: development of a multi-step surface reaction mechanism. *Top Catal*. 2011;54(13–15):845–858.
29. Hecht ES, Gupta GK, Zhu H, Dean AM, Kee RJ, Maier L, Deutschmann O. Methane reforming kinetics within a Ni–YSZ SOFC anode support. *Appl Catal A Gen*. 2005;295(1):40–51.
30. Zanfir M, Gavriilidis A. Catalytic combustion assisted methane steam reforming in a catalytic plate reactor. *Chem Eng Sci*. 2003;58: 3947–3960.
31. Ansys, Inc. *ANSYS FLUENT 13.0*. User's Guide. Canonsburg: Ansys, Inc., 2010.
32. Hutter C, Zenklusen A, Lang R, Rudolf von Rohr P. Axial dispersion in metal foams and streamwise-periodic porous media. *Chem Eng Sci*. 2011;66:1132–1141.
33. De Boor C. *A Practical Guide to Splines*. New York: Springer-Verlag, 1978.

Manuscript received Sept. 16, 2013, and revision received Jan. 9, 2014.